WELDING RESEARCH

SUPPLEMENT TO THE *WELDING JOURNAL*, MAY 1989

**Sponsored by the American Welding Society and the Welding Research Council**



# Control of Magnetic Permeability and Solidification Cracking in Welded Nonmagnetic Steel

*A variety of filler metals was determined to produce ferrite-free welds with a low risk of solidification cracking*

**BY B. F. DIXON**

ABSTRACT. This paper is concerned with the welding of austenitic steels for applications where the presence of delta ferrite in the final weld microstructure, normally considered essential for control of weld solidification cracking, cannot be tolerated.

An experimental program is described in which a high-manganese stainless steel base metal, proposed for structural applications in minesweeping ships, is welded using a range of filler metals at differing levels of dilution. Transvarestraint tests are conducted on the filler metals to rank them in order of sensitivity to solidification cracking. The results show that crack-free and ferrite-free welds are attainable over a wide range of compositions and welding parameters. Furthermore, it is demonstrated that one particular filler wire containing 7.6% manganese has exceptionally low sensitivity to solidification cracking while still providing a fully austenitic weld deposit.

*B. F. DIXON is with the Department of Defence Materials Research Laboratory, Defence Science and Technology Organization, Melbourne, Australia.*

## Introduction

It is particularly important that the hulls and deckboard equipment of minesweeper vessels do not have a magnetic "signature," since this property can readily trigger off mines equipped with the extremely sensitive magnetic sensing devices which are now available. Materials conventionally used in the construction of such vessels include wood and glass reinforced plastic and less often, aluminum alloys and austenitic stainless steels. Stainless steels offer significant advantages over the other materials because of their high strength, toughness, corrosion resistance and ease of fabrication. By virtue of their moderately high electrical resistivity, they also can be made to offer very small electrical inductance by the use of large degaussing coils, and so provide some immunity against a second type of mine sensor.

**KEY WORDS**

Austenitic Steels
Delta-Ferrite Effect
Magnetic Permeability
Solidification Crack
Nonmagnetic Steel
Mn Stainless Steel
7.6% Mn Filler Metal
Crack Sensitivity
Ferromagnetic Phases
Transvarestraint

The microstructural phases present in stainless steels are either ferromagnetic or paramagnetic. Martensite and ferrite are ferromagnetic, and so have high values of magnetic permeability (relative permeability $\mu_R > 230$), and they also exhibit magnetic hysteresis. Austenite is paramagnetic, which means that it does not exhibit any permanent magnetic properties and has almost negligible permeability values ($\mu_R \sim 1.00$ to 1.03). Since modern sensors can detect very low levels of magnetic permeability, it is essential to reduce the proportion of ferromagnetic phases in the microstructure of such steels to an absolute minimum. The potential application of these steels in minesweeper applications has stimulated the development of fully austenitic stainless steels and weld deposits.

A problem arises in the welding of austenitic stainless steels, however,

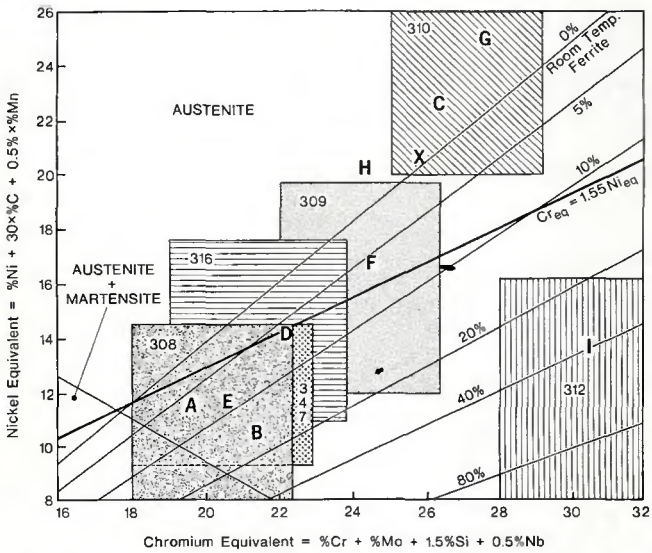


*Fig. 1—Region of the Schaeffler diagram, which shows the volume-percent of austenite, ferrite and martensite in a weld deposit of known composition. The shaded regions show the composition limits for some commercial stainless steels. Diagonal line ($Cr_{eq}$ = 1.55 $Ni_{eq}$) represents the approximate eutectic composition. Letters A–I represent the composition of filler metals used in this work and X represents the composition of the base metal*

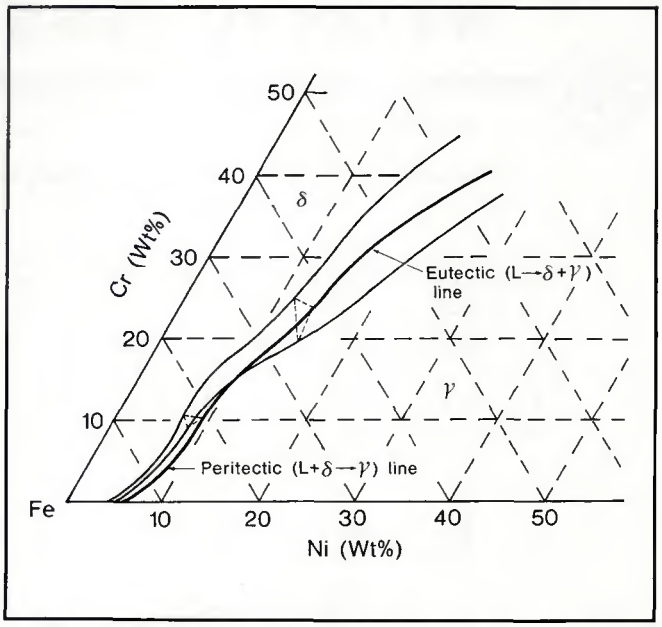


*Fig. 2—Part of the Fe-Cr-Ni ternary liquidus diagram showing the position of the eutectic/peritectic line. Moving away from the Fe-rich corner, alloys to the right of this line solidify as austenite and alloys to the left, as ferrite*

because the weld deposit microstructure is usually required to contain 3 to 8% ferrite, which is considered to be necessary for the control of weld metal solidification cracking. Although this ferrite content is small, it is sufficient to confer a measurable and unacceptably high ferromagnetic signature to a minesweeper hull. Furthermore, this ferrite can be responsible for accelerated corrosion, the formation of brittle sigma phase and deterioration in some weld mechanical properties.

It is therefore highly desirable to develop stainless steels, welding consumables and welding procedures which are capable of producing sound welds while ensuring that no ferrite is left in the final microstructure. The aim of the present work was to fully investigate the efficacy of one highly alloyed stainless steel which was developed for this application.

## Importance of Ferrite in Weld Metal

A recent review by the author (Ref. 1) has shown that a number of different explanations exist for the role played by ferrite in the suppression of weld metal solidification cracking. Until 10 to 15 years ago, for instance, it was universally held that the room-temperature ferrite content was of paramount significance for the following reasons:

1) Ferrite has a greater solubility for certain crack-promoting impurity elements, particularly sulfur and phosphorus, than does austenite.

2) Ferrite generates a substantial area of interphase boundary between ferrite and austenite, and this behaves as a "sink" to reduce the concentration of impurities at the austenite grain boundaries.

3) Ferrite controls the extent of austenite grain growth, large grains being associated with increased concentration of impurities and therefore increased sensitivity to cracking.

4) Ferrite causes a reduction in shrinkage stress because it has a lower coefficient of thermal expansion than austenite.

5) The austenite/austenite boundaries are more easily wetted by liquid impurities than the austenite/ferrite boundaries, and therefore, ferrite improves the ability of a weld to withstand the contraction forces which cause cracking.

The procedure usually adopted to achieve this 3 to 8% ferrite in the weld deposit involves the use of a diagram developed by Schaeffler (Ref. 2), part of which is reproduced in Fig. 1. This shows nickel equivalent ($Ni_{eq}$, calculated as %Ni + 30%C + 0.5%Mn) on the vertical axis and chromium equivalent ($Cr_{eq}$, calculated as %Cr + %Mo + 1.5%Si + 0.5%Nb) on the horizontal axis. The phase structure of the weld deposit is determined by plotting the composition of the weld deposit on this diagram. For example, a weld deposit composed entirely of AISI 310 stainless steel would have an austenitic microstructure containing up to 8% ferrite (see bottom right-hand corner of the shaded field labeled 310 in Fig. 1). Of course, the weld deposit composition is determined by the extent of base metal dilution and composition of the filler metal. Therefore, the usual procedure is to plot the composition of both filler and base metals on the Schaeffler diagram, construct a tie line between these points and mark off a distance along this line that is equivalent to the proportion of dilution. Practical examples of this will be given later.

Modifications to the Schaeffler diagram have involved expressions that attempt to include the effects of N, Cu, Co, Ti, Al and high values of Mn (Ref. 3).

The above explanations for the role of ferrite have recently been reviewed in the light of work by Masumoto and coworkers (Ref. 4) and others who have pointed out that cracking of concern here actually occurs during weld pool solidification, and therefore, room temperature ferrite may have at best limited relevance to crack sensitivity. The revised explanations take into account the different phase transformations that can occur when a particular weld undergoes solidification and subsequent cooling to room temperature. By reference to the Fe-Cr-Ni liquidus diagram shown in Fig. 2, for example, it is possible to determine whether a particular alloy of the three principal elements will solidify as austenite or ferrite. What is more, alloys having a composition close to the ternary eutectic/peritectic line may actually undergo solidification in both phases. This latter point can be illustrated with reference to a pseudo-binary phase diagram (Fig. 3) which shows that a three-phase field (area ABC in Fig. 3) exists immediately below the ternary eutectic line. It is widely held (Ref. 1) that alloys which undergo solidification through this three-phase

region have a reduced sensitivity to cracking. In fact, it is considered that the best resistance to cracking is achieved when solidification passes through the diagonal line (AB in Fig. 3) at a location close to A. The diagonal line ($Cr_{eq}$ = 1.55 $Ni_{eq}$) on the Schaeffler diagram in Fig. 1 represents the approximate eutectic composition for austenitic stainless steels.

It is believed that the solidification sequence undertaken by a particular weld metal can be determined by examination of its room temperature microstructure (Ref. 1) and examples are given in Figs. 3 and 4. At one extreme, if solidification occurs entirely in the austenite phase (say, $Cr_{eq}/Ni_{eq} < 1$) then the room temperature microstructure is completely austenitic—Fig. 4A. At the other extreme, if solidification occurs entirely in the ferrite phase ($Cr_{eq}/Ni_{eq} > 3$) some of this ferrite may subsequently transform to austenite and the microstructure will show ferrite with Widmanstatten austenite—Fig. 4E. The intermediate structures all show ferrite in a morphology which reflects their solidification sequences. Thus, if austenite solidifies first, but the composition is close to the ternary eutectic, then some interdendritic eutectic ferrite may occur—Fig. 4B. Should ferrite solidify first in a composition that is close to the eutectic composition, transformation of this ferrite to austenite will occur rapidly; for metal which solidifies entirely as ferrite, the transformation to austenite is likely to be incomplete and a lath ferrite structure results (Fig. 4D), while for metal which undergoes a phase transformation from ferrite to austenite during solidification, the ferrite dendrites are rapidly dissolved by austenite and a vermicular or skeletal ferrite structure results—Fig. 4C. It is this vermicular ferrite structure that is considered to be most desirable for control of cracking, since it reflects solidification through the diagonal line A-B on the pseudo-binary phase diagram—Fig. 3.

It should be noted that considerable overlap may occur between the five classifications defined here. For example, it is possible to identify vermicular and interdendritic eutectic ferrite in close proximity when a weld has undergone solidification through the three phases ($L + \delta + \gamma$), but where small variations in composition have been sufficient to give two distinct solidification sequences. Weld travel speed can also have an effect on the solidification sequence, because increased travel speeds can cause a shift from primary ferrite to primary austenite solidification in some welds (Ref. 1).

Various explanations for the mechanism of solidification cracking in steels have been outlined elsewhere (Ref. 5). It is generally considered that cracks form during the final stages of freezing when solid dendrites or cells are separated by thin films of liquid containing low melting-point segregates. The strains associated with solidification and subsequent thermal shrinkage are believed to rupture these films and thereby create cracks. When solidification occurs to a single phase, it is considered that these newly created cracks can travel with ease along the interdendritic spaces and grain boundaries (Ref. 6). When solidification occurs to two phases, however, the low melting point constituents become entrapped in the austenite.

Current explanations for the beneficial role of delta-ferrite in the control of solidification cracking, therefore, include all of the above given reasons to a degree, but emphasize the newer understandings which go further and take the solidification mechanisms into account. These new explanations include:

6) The solidification of austenite in spaces between the ferrite dendrites means that cracking is forced to travel along a tortuous ferrite/austenite interface which offers increased resistance to crack growth.

7) Solidification in only one phase (either ferrite or austenite) causes cracking to extend along grain boundaries which provide smooth, easy paths for crack

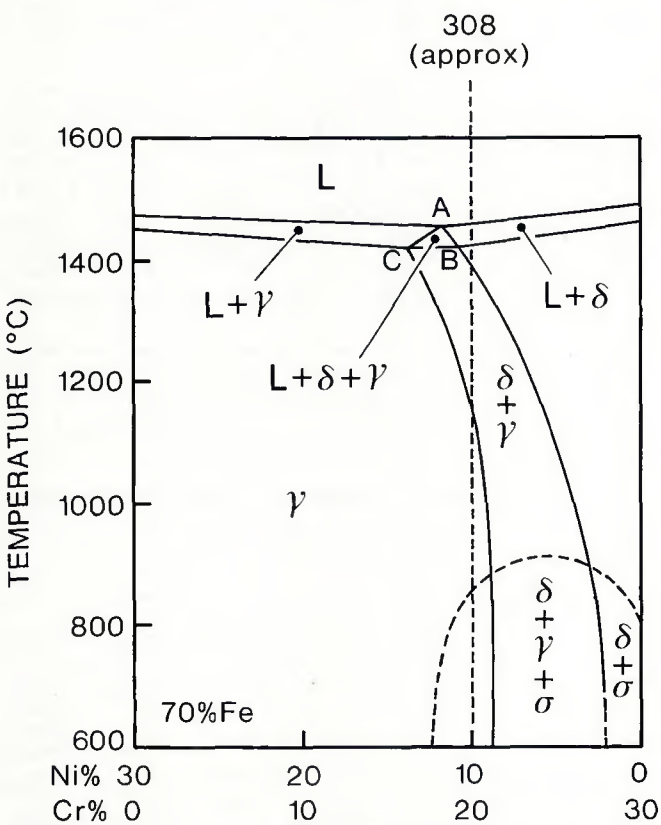


*Fig. 3—Pseudo-binary phase diagram at 70% iron. Sensitivity to cracking is considered to be lowest when solidification occurs through the diagonal line AB*

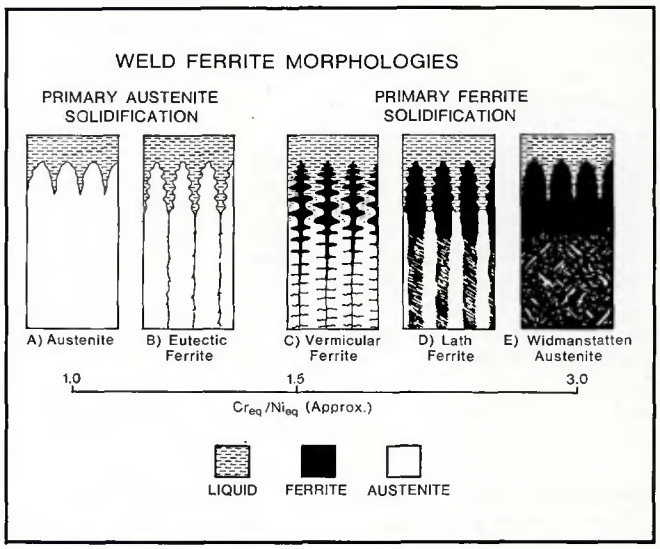


*Fig. 4—Diagram showing different solidification sequences for differing ratios of $Cr_{eq}/Ni_{eq}$*

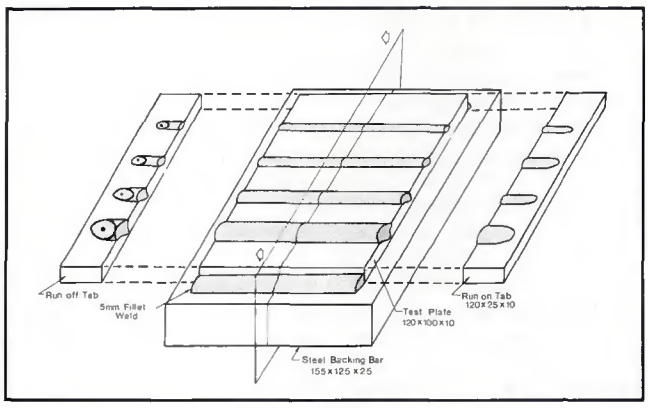


*Fig. 5 — Design of the bead-on-plate tests used in this work. The plane through the center of this plate represents the location of metallographic sections*

growth. The existence of a second phase controls grain boundary straightening and, in cases where the second phase actually crosses grain boundaries, impedes the growth of cracks.

8) Alloys that solidify as a ternary eutectic are considered to be more capable of dissolving harmful impurities and are believed to have a lower thermal expansion coefficient than austenite alone.

It can be deduced from the above that control of solidification cracking is currently being achieved by manipulation of the welding process to achieve initial solidification of ferrite followed by solidification of ferrite and austenite. Coincidently, this usually results in a room temperature microstructure containing 3–8% ferrite, and it is noted (Fig. 1) that most of the commercial austenitic weld filler metals have compositions close to the eutectic/peritectic line.

## Alternative Techniques for Control of Weld Cracking

With the benefit of the greater understanding intrinsic to these newer explanations, namely that composition to suppress cracking is not directly related to the room temperature microstructure, it should be possible to control solidification cracking without the need for resorting to compositions that produce delta ferrite at room temperature. Techniques which have been considered include: 1) use of alloying elements that promote ferrite at higher temperatures and austenite at lower temperatures; 2) solution heat treatment to dissolve ferrite after welding and reduction of impurity levels so that the need for high-temperature ferrite is reduced; 3) electromagnetic stirring, arc pulsing and other procedures that interrupt the dendrite growth pattern and restrict the growth of austenite grains; and 4) control of cooling rates to maximize the formation of austenite.

The present work, therefore, sought to investigate the first of these techniques for control of cracking (*i.e.*, alloy content control) by using welds which contain increasing levels of manganese and nitrogen. It has been suggested (Ref. 7) that increasing the level of manganese in the weld deposit can produce sound, ferrite-free welds. Reasons for this include:

1) Manganese may promote ferrite at higher temperatures and austenite at lower temperatures. Kujanpaa (Ref. 8) found that 18 Cr, 8 Ni, 6 Mn-type welds in fully austenitic stainless steels produced a primary ferritic solidification mode in spite of having very low finite contents in the room temperature microstructure.

2) The presence of substantial amounts of manganese enables sulfur to be held as manganese sulfide. This melts at higher temperatures than does crack-promoting nickel sulfide which is said to form in stainless steels having conventional composition (Ref. 9).

A two-stage approach was adopted in this study. Firstly, in order to identify the effect of composition and welding parameters on microstructure, a number of commercial gas metal arc (GMA) filler metals were welded onto highly restrained stainless steel plates of the specified composition. A range of power inputs was used at the same nominal heat input to provide a gradation of compositions and pool profiles for each wire. The second stage involved transvarestraint testing of the filler metals in order to rank them in order of sensitivity to solidification cracking.

## Experimental

### Bead-on-Plate Tests

Gas metal arc welding with 1.2-mm (0.045-in.) diameter austenitic welding electrodes was used to produce the bead-on-plate test specimens. These were highly restrained by welding onto steel backing bars, as shown in Fig. 5. Composition of the test plate and all electrodes used are given in Table 1 and these are set out on the Schaeffler diagram in Fig. 1. The five sets of welding parameters used (Table 2) were selected to provide five sets of current, voltage and travel speed values to give a range of weld dilutions, penetrations and weld pool profiles, but maintaining the same heat input.[1] In all welds, the torch height was maintained at 22 mm (0.9 in.) and the angle of the torch 15 deg from the vertical pointing in the direction of torch travel. Argon-based shielding gas was used, regulated to flow at 15 L/min (7 cfh) for currents up to 250 A and 20 L/min (9.4 cfh) for higher currents. About 20°C (68°F) preheat was used for each weld. A synergic[2] pulsed GMA welding machine was used for all welds in order to provide accurate control over welding

[1] *Calculated as:* $HI = (I.V/1000.u)\ (kJ/mm^{-1})$
*where* $I$ = *current (A)*
$V$ = *voltage (V)*
$u$ = *travel speed* $(mm/s^{-1})$

**Table 1—Composition of Base Metal and Electrode Wires**

| GMA Welding Electrodes | C | Si | Mn | S | P | Ni | Cr | Mo | Ti | V | Nb | N |
|---|---|---|---|---|---|---|---|---|---|---|---|---|
| A (18/8/1) | 0.085 | 0.49 | 0.61 | 0.024 | 0.022 | 8.73 | 18.72 | 0.06 | 0.01 | 0.01 | 0.76 | 0.068 |
| B (Type 308L) | 0.027 | 0.44 | 1.66 | 0.016 | 0.018 | 10.00 | 20.74 | 0.02 | 0.01 | 0.02 | 0.01 | 0.053 |
| C (25/20) | 0.082 | 1.04 | 0.65 | 0.022 | 0.026 | 20.03 | 24.53 | 0.09 | 0.77 | 0.06 | 0.05 | 0.015 |
| D (Type 316L) | 0.018 | 0.79 | 1.88 | 0.001 | 0.022 | 12.60 | 18.65 | 2.31 | 0.01 | 0.03 | 0.02 | 0.021 |
| E (Type 347) | 0.035 | 0.71 | 1.82 | 0.007 | 0.014 | 9.89 | 19.35 | 0.05 | 0.02 | 0.02 | 0.74 | 0.042 |
| F (Type 309) | 0.072 | 0.84 | 2.06 | 0.007 | 0.026 | 13.55 | 23.11 | 0.11 | 0.01 | 0.05 | 0.01 | 0.032 |
| G (Type 310) | 0.12 | 0.43 | 1.72 | 0.002 | 0.011 | 20.55 | 25.63 | 0.03 | 0.01 | 0.07 | 0.01 | 0.063 |
| H (Special) | 0.015 | 0.57 | 7.62 | 0.004 | 0.019 | 15.93 | 20.36 | 2.86 | 0.01 | 0.06 | <0.01 | 0.20 |
| I (Type 312) | 0.12 | 0.40 | 1.78 | 0.005 | 0.016 | 9.16 | 29.73 | 0.06 | 0.01 | 0.13 | <0.01 | 0.078 |
| Stainless steel base metal | 0.043 | 0.63 | 5.45 | 0.005 | 0.014 | 16.32 | 21.59 | 3.23 | 0.01 | 0.04 | 0.20 | 0.35 |

parameters and to ensure that the spray transfer mode was always achieved. Weld travel speed was monitored continuously during each test.

The test plate design (Fig. 5) consisted of a test plate 120 × 100 × 10 mm (4.7 × 4 × 0.4 in.) welded with AISI 309 filler metal to a backing bar 155 × 125 × 25 mm (6 × 5 × 1 in.) by two 5-mm (0.2-in.) fillet welds such that the rolling direction of the plate was at right angles to the direction of welding during the tests. In addition, run-on and run-off tabs (both 120 × 25 × 10 mm) were tack welded to the test plate to ensure that welding conditions were stable during each test, and to allow for minor adjustments of the wire feed rate before welding of the test plate was commenced. After each weld series, the test plate was removed from the backing bar by cutting through the restraining welds, and then radiographed to identify any defects. The plate was then sectioned along its center, as shown in Fig. 5, to provide a representative cross-section of each weld. These weld sections were subsequently prepared for both macroscopic and microscopic metallographic examination and each weld deposit was chemically analyzed. In addition, any indications of defects identified by radiography were sectioned for metallographic examination.

The sections were etched using two techniques. The first was an electrolytic etch in a bath containing 40-g NaOH in 200-mL water. Etching time was 20 s at 10-V DC. This is a reliable and commonly used etchant for the identification of ferrite; however, because it does not expose the primary solidification structure, it is unable to distinguish between interdendritic and vermicular forms of ferrite. The second procedure was a color deposition etch using 20-mL HCl, 80-mL $H_2O$ and 1- to 2-g $K_2S_2O_5$. The solution was freshly prepared and nonmetallic tongs used at all times. Etching times were 5 to 10 s. This etchant is less consistent in results than the electrolytic etch, but it is capable of revealing both the ferrite, if present, and the primary solidification structure.

To examine the influence of multipass welding on weld dilution, microstructure and crack sensitivity, an additional series of tests was conducted. For this work, each test plate contained four welds, one weld bead on top of the other, with welding conditions selected so that each pass contained about 50% dilution from the preceding pass. Thus, the first pass typically obtained 50% of its composition from the base metal, the second pass 25%, the third pass 12%, and the fourth pass 6%. The power input for each weld was about 11.2 kW. Only certain weld filler metals were used in this work, namely the AISI 308, 310 and 312, because of their significant compositions. The 308 filler metal produces welds containing about 15% room temperature ferrite, while the 310 is highly austenitic and the 312 is highly ferritic. Thus, these weld deposits showed a wide range of compositions and microstructures.

**Table 2—Average Welding Parameters for Bead-on-Plate Weld Passes**

| Pass Code | Wire Feed Speed (mm/s) | Current (A) | Voltage (V) | Tractor Speed (mm/s) | Arc Gap (mm) |
|---|---|---|---|---|---|
| A | 67.8 | 123 | 27.6 | 1.7 | 11 |
| B | 102.8 | 186 | 32 | 2.9 | 16 |
| C | 137.5 | 250 | 35.5 | 4.4 | 18 |
| D | 170.5 | 312 | 38.6 | 6.1 | 19 |
| E | 204.3 | 374 | 41.9 | 7.8 | 19 |

### Transvarestraint Testing

The transvarestraint test (Fig. 6) is based on a machine developed by Brockhurst and Muir (Ref. 10) from the original Murex test (Ref. 11). The test operates by three-point bending of a test plate, as it is being welded, over a gable-shaped, roof-top former. As illustrated in Fig. 6, the test plate is bent across the line of the weld so that cracks are encouraged to travel along it. In the present apparatus (Ref. 12), the bending force was applied through a loading yoke driven by a pneumatic ram whose velocity was regulated precisely by hydraulic cylinders. This control system enabled the required velocity to be reached almost instantaneously from rest and the total displacement to be accurately controlled.

Test specimen consisted of a carbon-manganese steel base plate 76 × 305 × 19 mm (3 × 12 × 0.75 in.) with a 50- × 10-mm (2- × 0.4-in.) groove removed from across its center. This groove was filled with two shaped coupons of the base metal under investigation (Fig. 7), and were welded in place. The resulting test configuration has significant advantages over the traditional transvarestraint test plate in that it incorporates a realistic single-V joint preparation with a 2-mm (0.08-in.) root opening and, because the test coupons can slide across the base plate, straining is largely tensile across the weld. Welding was again carried out using 1.2-mm-diameter wire and argon-based shielding gas. Welding parameters were 360 A, 34 V and 4.8-mm/s (11-ipm) travel speed.

Tests were conducted at a fixed ram velocity of 5 mm/s (12 ipm) and two levels of ram displacement (0.4 and 1.1 mm). The extent of cracking in each test plate was assessed by two techniques: firstly, by measuring the total crack length on six polished sections, and secondly, by counting the number of cracks on radiographs of three segments taken from the weld. Both techniques are described in Ref. 13. Scanning electron microscopy was carried out on selected solidification crack fracture surfaces which occurred during transvarestraint testing.

## Results

For the bead-on-plate tests, no evidence of cracking was found on any of the radiographs and only minor cracking was found on the sections examined. Macrophotographs of welds representative of the five sets of welding parameters are shown in Fig. 8. All welds had large grain sizes.

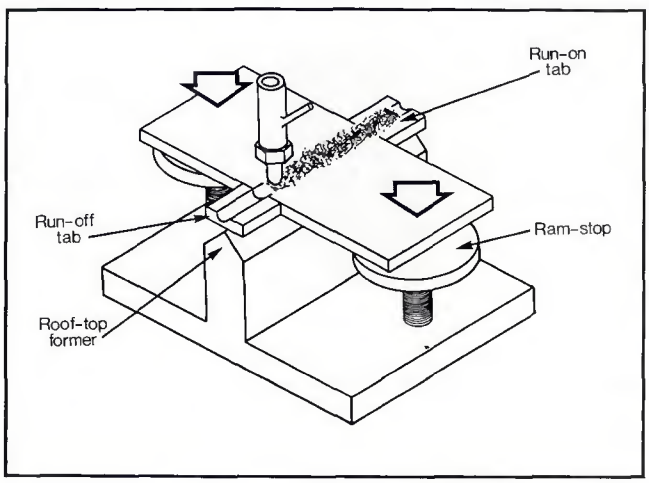


*Fig. 6—Fundamental features of the transvarestraint test. Rapid strain is applied across the weld bead by three-point bending of the test plate over a gable-shaped roof-top former. In this work, both the rate of bending and the total bend angle were accurately controlled. These were measured as velocity and displacement of the loading ram respectively*

[2] *Microprocessor-controlled welding equipment with feedback control over wire feed speed.*

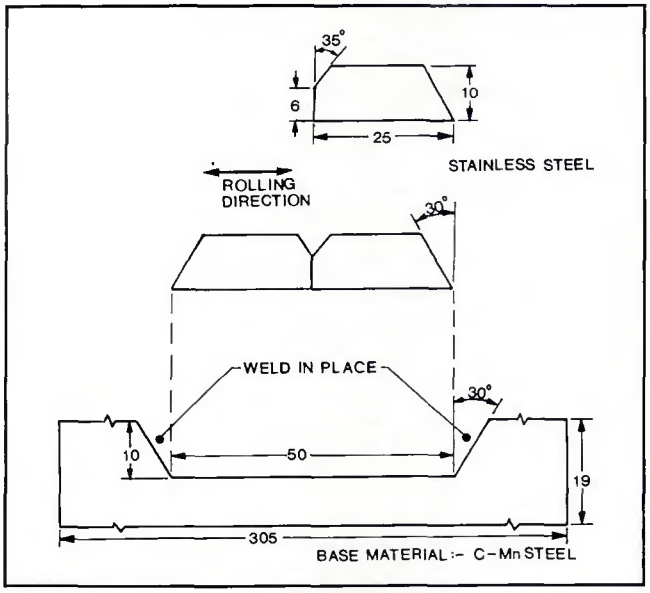


*Fig. 7—Detail of the transvarestraint test plate used for this work. Two shaped specimens of the base metal under investigation were welded to a carbon-manganese base plate as shown. The test weld was then conducted along the butt joint between these two specimens. Dimensions are in mm*

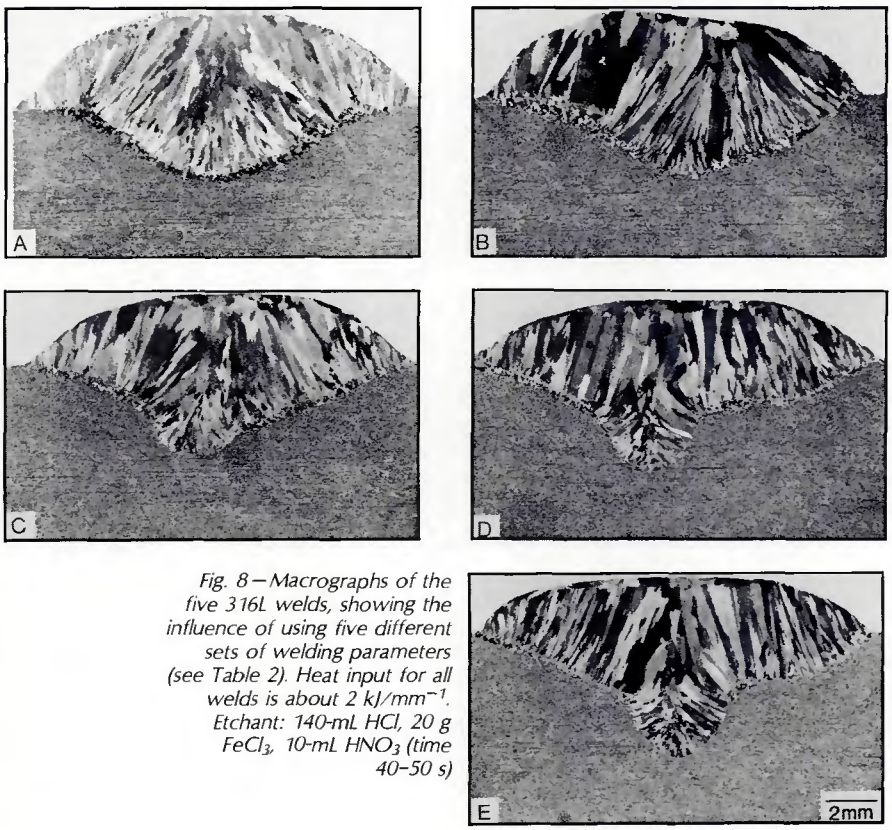


*Fig. 8—Macrographs of the five 316L welds, showing the influence of using five different sets of welding parameters (see Table 2). Heat input for all welds is about 2 kJ/mm$^{-1}$. Etchant: 140-mL HCl, 20 g $FeCl_3$, 10-mL $HNO_3$ (time 40–50 s)*

The depth of penetration for all welds was important because this was related to the thermal shrinkage strains experienced by the weld. The value of penetration for each weld was determined from its macrophotograph by constructing a line across the weld between the unwelded plate surfaces on each side to distinguish the crown (above) from the penetration (below). The depth of penetration was given by the perpendicular distance from this line to the deepest point on the weld toe, and it ranged from 1 to 6 mm (0.04 to 0.24 in.).

The degree of base metal dilution in each weld was determined by tracing the weld profile onto a fine grid, and was given as the area of penetration below the datum line and as a fraction of the total weld cross-section. When values of dilution for each of the welds are plotted against power (Fig. 9), it is seen that, despite some scatter, dilution increases with power in a linear manner. The range of dilution values achieved in this work extended from 12 to 61%, with 50% dilution occurring at about 11.2 kW power input.

Each weld deposit was analyzed chemically and variations in the main alloying elements with base metal dilution are shown in Fig. 10. It can be seen that, allowing for scatter, a near linear relationship generally exits between the amount of each element and the dilution of the weld pool. Some considerable scatter of results occurred with carbon in particular, and this was attributed to inaccuracies intrinsic to chemical analysis. The most significant anomaly that occurred in these

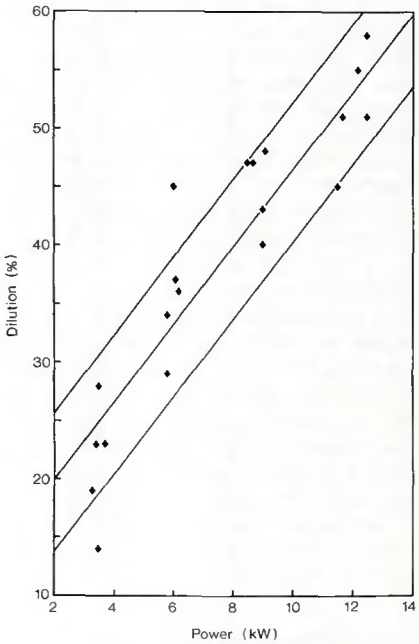


*Fig. 9—Values of weld metal dilution (in percentage) against power. Bands show the approximate range of results*

results was that a large portion of the nitrogen present in the high-nitrogen filler metal (Electrode H) did not transfer to the weld deposit. Some loss of manganese also occurred with this electrode.

Micrographs showing fully austenitic weld metal, Widmanstatten austenite and examples of so-called interdendritic, vermicular and lath ferrite are given in Fig. 11. Vermicular ferrite is assumed to be clearly distinguishable from interdendritic ferrite because it occurs along the primary dendrite axes, whereas interdendritic ferrite occurs between the primary dendrites. With the exception of welds deposited using Electrodes G and H, no sample was completely free of ferrite because small zones of ferrite could always be found at some of the triple points between dendrites that were otherwise completely austenitic. Even Electrode C (which is close to Electrode G on the Schaeffler diagram) produced some ferrite, most likely due to the fact that it contains 0.8% Ti, which is a strong ferrite stabilizer.

The ferrite morphologies occurring in a particular weld often varied from one zone to another. In particular, it was common for interdendritic ferrite to occur in the cellular region of a weld (close to the fusion boundary), while vermicular ferrite occurred in the region around the center of the same weld. It was also common to find vermicular, and occasionally lath, ferrite in isolated grains around a weld deposit which largely contains interdendritic ferrite.

The ferrite formations occurring in each weld are plotted using the axes of the Schaeffler diagram in Fig. 12. In this diagram, the deposits were classified as "ferrite-free" if they contained ferrite only as small, spherical, interdendritic particles on the section surface. This low-ferrite content cannot be detected by sensing equipment. The composition of each deposit was determined from the filler metal composition and base plate dilution, as described previously. If more than one structure occurred in any weld deposit, then the convention adopted in construction of Fig. 12 was to plot the most highly ferritic of the structures present. In other words, the structure plotted was that closest to the bottom right-hand corner in Fig. 12.

The ferrite content of each weld deposit as measured by the popular Severn ferrite indicator is plotted using the

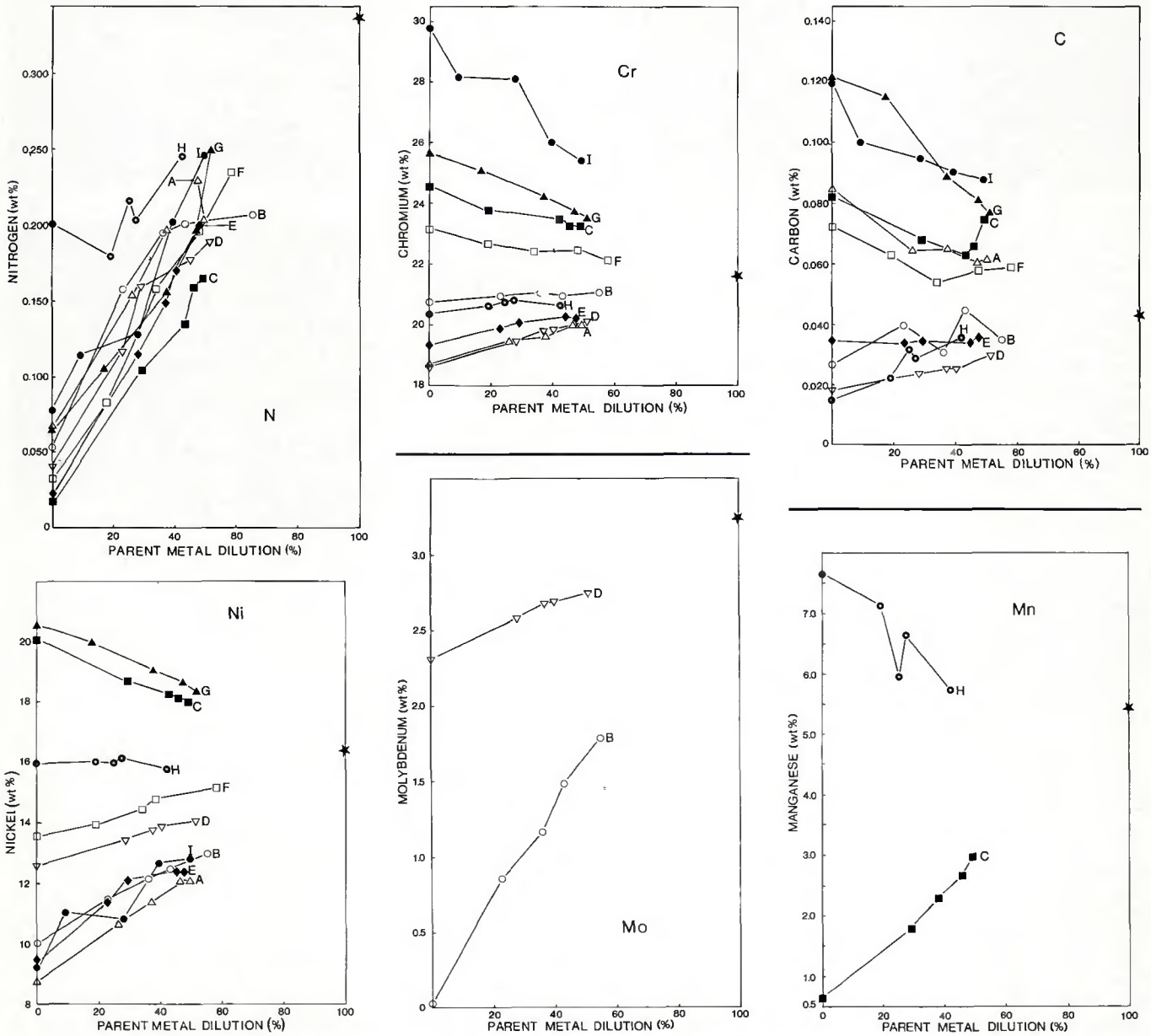


*Fig. 10—Relationship between composition and dilution for each weld deposit. Star symbols (*) represent the base metal composition for each element*

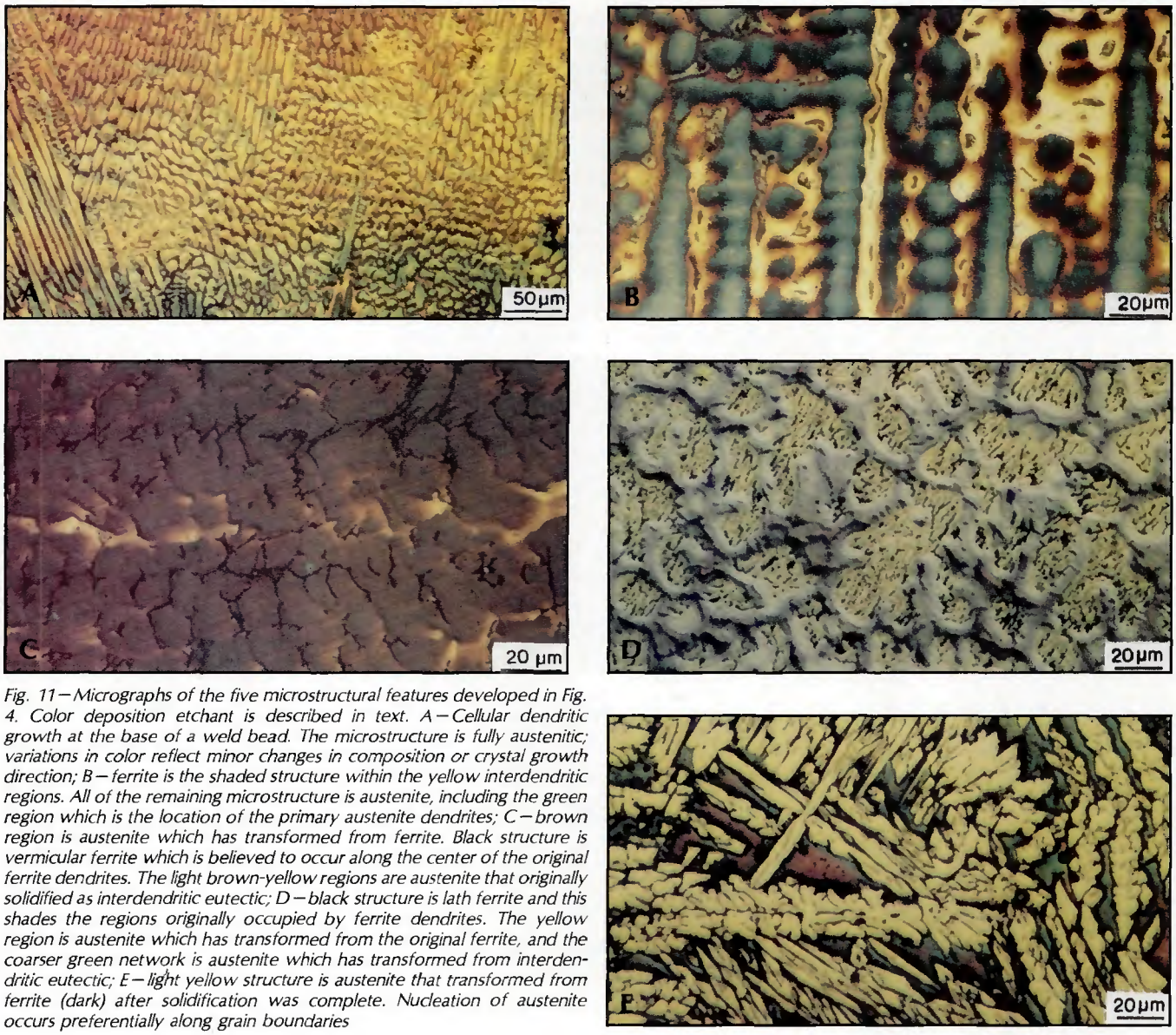


*Fig. 11—Micrographs of the five microstructural features developed in Fig. 4. Color deposition etchant is described in text. A—Cellular dendritic growth at the base of a weld bead. The microstructure is fully austenitic; variations in color reflect minor changes in composition or crystal growth direction; B—ferrite is the shaded structure within the yellow interdendritic regions. All of the remaining microstructure is austenite, including the green region which is the location of the primary austenite dendrites; C—brown region is austenite which has transformed from ferrite. Black structure is vermicular ferrite which is believed to occur along the center of the original ferrite dendrites. The light brown-yellow regions are austenite that originally solidified as interdendritic eutectic; D—black structure is lath ferrite and this shades the regions originally occupied by ferrite dendrites. The yellow region is austenite which has transformed from the original ferrite, and the coarser green network is austenite which has transformed from interdendritic eutectic; E—light yellow structure is austenite that transformed from ferrite (dark) after solidification was complete. Nucleation of austenite occurs preferentially along grain boundaries*

axes of the Schaeffler diagram in Fig. 13. It is evident from Figs. 12 and 13 that, by comparison with the original Schaeffler diagram, the 0% ferrite line appears to have been displaced towards the chromium equivalent axis for this high-manganese base metal.

The results of transvarestraint testing are presented in Fig. 14. It can be seen that the testing procedure was able to rank candidate consumables at 1.0-mm displacement by the crack length technique and at both 0.4- and 1.0-mm displacement by the crack number technique. Approximate rankings were (from most- to least-crack sensitive, and using AISI designations where applicable): 309, 310, 347, 25 Cr/20Ni/0.7 Ti, 308, 316, 19 Cr/9 Ni/0.8 Nb, 20 Cr/16 Ni/8 Mn/3 Mo, and 312. All of the weld deposits produced in this series of tests were subjected to metallographic examination, and the only weld that contained vermicular ferrite, and therefore, believed to have solidified as ferrite phase, was that produced by Electrode I. This showed a microstructure having about 90% of its ferrite content as vermicular ferrite and about 10% as lath ferrite. Weld metal ferrite content obtained using Electrode I was 7.5–10% as measured by the Severn ferrite indicator. All other deposits registered less than 1.5% ferrite.

A scanning electron micrograph of the base of one of the solidification cracks produced during transvarestraint testing of Electrode H is shown in Fig. 15. This shows regions of flat or angular features associated with two phase ($L \rightarrow \gamma$) solidification and regions of dendritic features associated with three phase ($L \rightarrow \gamma + \alpha$) solidification (Refs. 1, 14). Furthermore, close examination of the dendritic regions (Fig. 16) revealed lines of rough features along the edge of each dendrite. Energy dispersive x-ray analysis of these rough features (Fig. 17) showed them to be enriched in the elements Si, Mo, Cr, and (to some extent) Ni and Mn by comparison with the smooth surface.

## Discussion

Metallography of the weld deposits has provided evidence of the three ferrite morphologies: interdendritic, vermicular and lath. However, there is clear evidence in this work that interdendritic ferrite may occur in regions of primary ferrite solidification and some evidence of primary austenite and primary ferrite solidification occurring in adjacent grains. This means that the explanations in Fig. 4 for each of the three ferrite structures is an oversimplification.

Results of the bead-on-plate tests show that, for this particular base metal, it is possible to produce virtually ferrite-free welds using a range of commercial filler

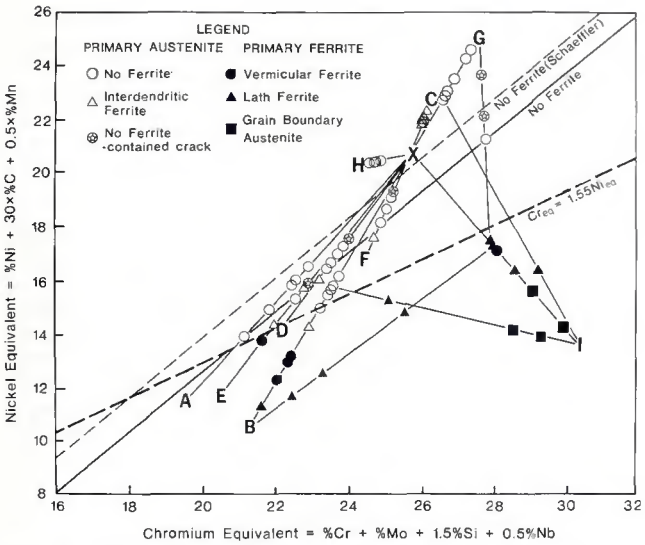


*Fig. 12 — Schaeffler diagram showing the composition and microstructure of weld deposits*

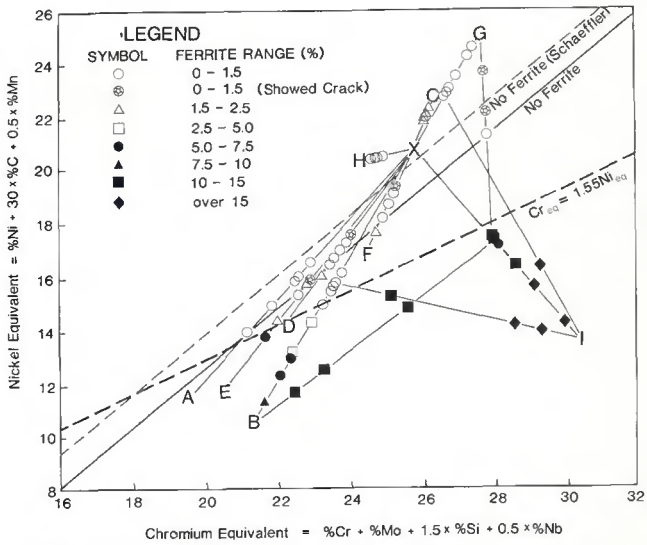


*Fig. 13 — Schaeffler diagram showing the ferrite content of each weld deposit as measurement by the Severn ferrite indicator*

metals and with low risk of solidification cracking. This work shows that control of power input is a reliable means of predicting base metal dilution and therefore, the composition and microstructure of the weld deposit. In addition, it appears that control of both ferrite content and solidification cracking can be achieved simultaneously for a number of commercial filler metals by simply choosing an optimum power input range for the consumable selected. These optimum power input ranges, presented in Table 3, have been determined from an analysis of the results presented in Figs. 12 and 13, and the data in Table 2.

Results of transvarestraint testing have enabled the candidate welding consumables to be ranked in order of crack sensitivity with the highly austenitic filler metals (309 and 310) being the most sensitive and the only deposit to solidify as delta ferrite (312) being the least sensitive. This last result is consistent with the conventional wisdom that weld deposits having vermicular ferrite as a room temperature microstructure exhibit reduced sensitivity to cracking.

The work has shown a significant benefit in using the high-manganese filler wire (Electrode H) for fabrication applications where the presence of ferrite cannot be tolerated. The room-temperature weld deposits produced by this filler wire were fully austenitic over a wide range of power inputs used in the bead-on-plate tests, and transvarestraint tests clearly showed this filler metal to have a very low sensitivity to solidification cracking. In fact, by comparing the transvarestraint test results (Fig. 14) for Electrode H with those for Electrodes F and G, it becomes clear that the high-manganese electrode has a remarkable attribute, the exact nature of which requires further investigation. As expected, Electrodes F and G were sensitive to cracking because Electrode F had only a small amount of interdendritic ferrite and Electrode G was fully austenitic. However, Electrode H was highly resistant to cracking even though it has a fully austenitic microstructure.

This exceptional performance cannot be directly attributed to the presence of nitrogen in the filler metal since chemical analysis has shown that a large fraction of

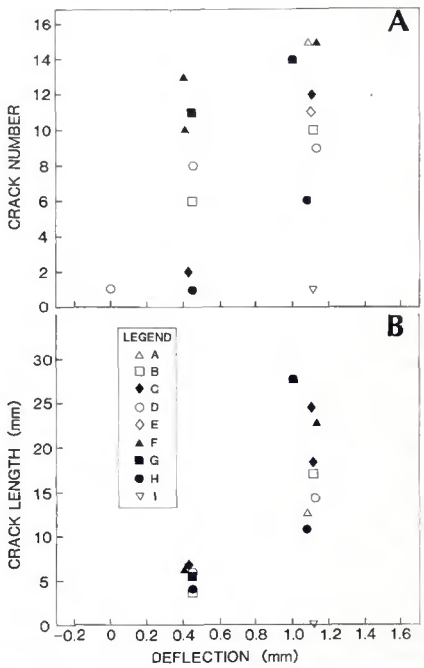


*Fig. 14 — Results of transvarestraint testing at constant velocity (5 mm/s) and two levels of displacement (0.4 mm and 1.1 mm). Extent of cracking is determined by: 1) total crack number on radiographed sections, and 2) total crack length on transverse sections*

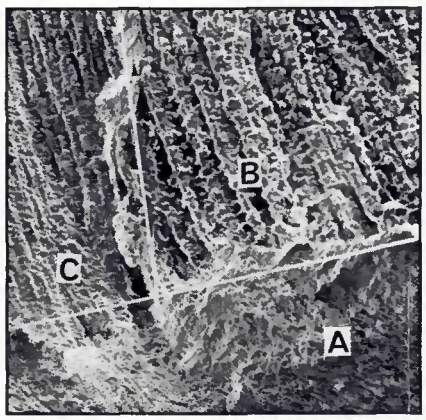


*Fig. 15 — Scanning electron micrograph of the base of cracking produced during transvarestraint testing of Electrode H. The three regions identified in the micrograph and their supposed causes are: A — Ductile dimples resulting from opening of the crack at room temperature; B — dendritic features associated with solidification of liquid to both ferrite and austenite; C — grain boundary features associated with solidification of liquid to austenite only*

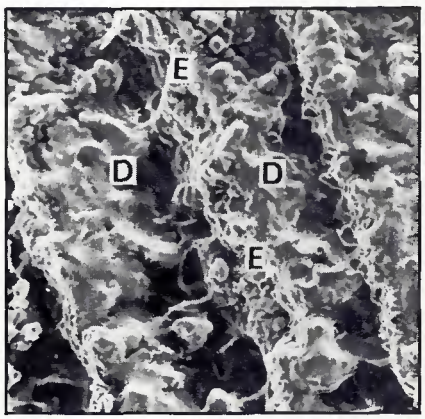


*Fig. 16 — Detail of the dendritic region (B) in Fig. 15, showing the rough features (E) along the edge of otherwise smooth dendrites (D)*

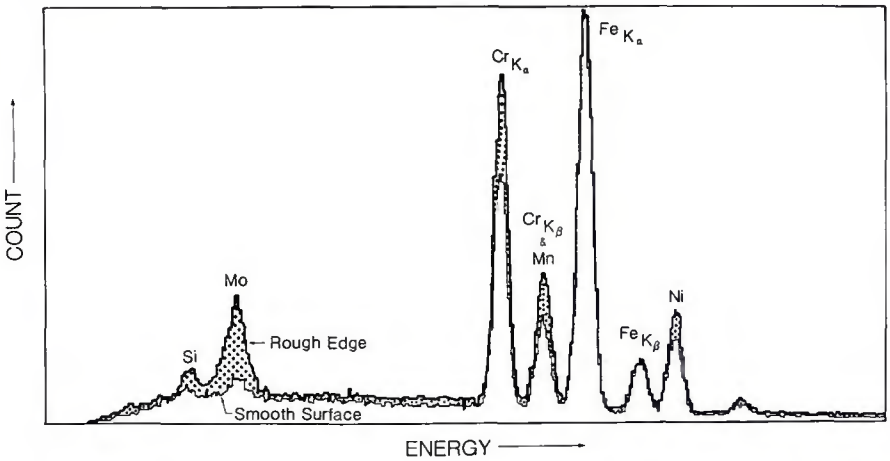


*Fig. 17 — Energy dispersive x-ray analysis of rough (E) and smooth (D) features in Fig. 16. The rough features are enriched in the ferrite promoting elements Si, Mo and Cr and (to a small extent) in the austenite promoting element Ni. The degree of enrichment is shown shaded*

**Table 3—Conditions Necessary to Control Both Cracking and Ferrite for Bead-on-Plate Welds**

| Electrode | A | B | C | D | E | F | G | H | I |
|---|---|---|---|---|---|---|---|---|---|
| Minimum power input required to avoid ferrite (kW) | NF[a] | 9 | SF[b] | 5.8 | 5.8 | 5.8 | NF | NF | AF[c] |
| Maximum power input to avoid cracking (kW) | NC[d] | NC | NC | 12.5 | 11.5 | 12.5 | NC | NC | NC |

(a) NF — All welds contained no ferrite. (c) AF — All welds contained ferrite.
(b) SF — Most welds contained ferrite. (d) NC — No welds contained cracks.

the nitrogen did not transfer to the weld deposit — Fig. 10.

Evidence about the beneficial influence of manganese provided by this work is complementary. One explanation is provided by Figs. 12 and 13, which indicates that high-manganese levels in the base metal have caused the 0% ferrite line to be shifted towards the chromium equivalent axis while the eutectic line appears to remain stationary. This suggests that manganese encourages the formation of room temperature austenite. Thus, the weld deposits solidifying as ferrite are likely to contain more austenite in the room-temperature microstructure if high-manganese base and filler metals are used.

Further supporting evidence for this effect of manganese is provided by the fractographic evidence in Figs. 15 and 16. This shows both angular and dendritic features at the base of an artificially induced crack, and therefore, suggests that solidification has occurred in primary austenite and primary ferrite modes simultaneously. It can be deduced from this that manganese has encouraged solidification to initiate as ferrite and then allowed this ferrite to transform completely to austenite during the final stages of freezing and subsequent cooling. In other words, the eutectic line in Figs. 12 and 13 has actually been shifted away from the chromium.

When these two explanations are combined, it can be concluded that manganese is beneficial because it encourages the solidification of ferrite at high temperatures and rapid transformation to austenite at lower temperatures.

Energy dispersive x-ray analysis of the dendritic features (Fig. 17) shows that considerable enrichment of the ferrite-promoting elements (Si, Mo and Cr) has occurred along rough edges on the otherwise smooth dendrites. These edges may be the sites of original ferrite dendrites and other rough appearance may result from high-temperature rupture of the solid vermicular ferrite arms. Since the rupture of these arms would provide considerably greater resistance to the growth of solidification cracks than smooth liquid films, this suggests an explanation for the beneficial effect of vermicular ferrite additional to those described in the introduction. That is, vermicular ferrite can hamper the growth of cracks by forming solid-solid bonds across potential crack paths. It is noted that evidence conflicting with this explanation is provided by the measurable enrichment of austenite promoting Ni, which also occurred along the same rough edges.

## Conclusions

1) For the high-manganese, austenitic stainless steel base metal under investigation, it is possible to deposit substantially ferrite-free welds, using a range of commercial filler metals, with a low risk of solidification cracking.

2) Of those electrodes which were investigated, the optimum properties were obtained by using Electrode H, which contained 7.6% Mn.

3) Manganese is considered to be beneficial because it encourages the solidification of ferrite at high temperatures and rapid transformation to austenite at lower temperatures. This solidification sequence is known to produce the best resistance to solidification cracking.

4) Initial solidification of delta-ferrite in austenitic weld deposits may hamper the development of solidification cracks by forming solid-solid bonds across potential crack paths.

*References*

1. Dixon, B. *Weld Metal Solidification Cracking in Austenitic Stainless Steels.* To be published in Australian Welding Research.

2. Schaeffler, A. L. 1949. Constitution diagram for stainless steel weld metal. *Met. Prog.* 56:680 and 680-B.

3. Olson, D. L. 1985. Prediction of austenitic weld metal microstructure and properties. *Welding Journal* 64(10):281-s to 295-s.

4. Masumoto, I., Tamaki, K., and Kutsuna, M. 1972. Hot cracking of austenitic steel weld metal. *Trans. Jap. Weld. Soc.* 41:1306–1314.

5. Dixon, B. F. 1981. Weld metal solidification cracking in ferritic steels — a review. *Aust. Weld. J.* 26:23–30.

6. Matsuda, F, Nahagama, H., Katajana, S., and Arata, Y. 1982. Weld metal cracking and improvement of 25% Cr-20% Ni (AISI 310S) fully austenitic stainless steel. *Trans. Jap. Weld. Soc.*, pp. 41–58.

7. Araki, Y., Sano, H., Kominami, M., and Oikawa, H. 1982. Study on the Cr-Ni austenitic filler metal containing Mn. *Trans. Jap. Weld. Soc.* 13:32–40.

8. Kujanpaa, V. P. 1985. Effects of steel type and impurities in solidification cracking of austenitic stainless steel welds. *Metal Construction* 17:40R–46R.

9. Matsuda, F., Nakagawa, H., Katayama, S., and Arata, Y. 1982. Solidification crack susceptibility in weld metals of fully austenitic stainless steels (Report VII) — effect of Mn and N on solidification crack resistance. *Trans JWRI* 11:79–85.

10. Brockhurst, P. T., and Muir, H. 1965. Hot cracking of welds. *Welding Fabrication and Design* 9(9):80–86.

11. Jones, P. W. 1959. An investigation of hot cracking in low-alloy steel welds. *British Welding Journal* 6:282–290.

12. Dixon, B., Baldwin, N., and Connell, D. Precision control of the transvarestraint test. To be published.

13. Dixon, B. F. 1984. Cracking in the transvarestraint test, Part I: A new procedure for assessment of cracking. *Metal Construction* 16:86–90.

14. Matsuda, F., Nahagawa, H., Vehara, T., Katayama, S., and Arata, Y. 1979. A new explanation for role of delta-ferrite improving weld solidification crack susceptibility in austenitic stainless steel. *Trans. JWRI* 8:105–112.